Visible-light Z-scheme MoS_2/CdS heterostructure for photocatalytic degradation of organics and surfactants in produced water

Y. Li [a], X. Chen [a], Z. Wang [a,*]
[a] *CNPC Research Institute of Safety & Environment Technology Corporation, Beijing, 102206, China*

Produced water from oil and gas operations contains persistent organic compounds and surfactants that are difficult to remove using conventional treatment. In this study, novel MoS_2/CdS Z-scheme heterostructures were synthesized and systematically characterized. Characterizations confirmed the intimate interfacial integration of ultrathin MoS_2 nanosheets on CdS nanorods, leading to enhanced surface area (68.5 m^2/g for 5%-MC vs. 42.1 m^2/g for CdS) and broadened visible-light absorption. The optimal composite, containing 5 wt% MoS_2, exhibited superior photocatalytic activity toward phenol and sodium dodecyl sulfate (SDS) degradation under visible light. Phenol degradation reached 95.2% with a pseudo-first-order rate constant of 0.0245 min^{-1}, approximately 4.9 and 8.2 times higher than pure CdS (0.0050 min^{-1}) and MoS_2 (0.0030 min^{-1}), respectively. For SDS, the same composite achieved 81.5% total organic carbon removal within 120 minutes. Photoelectrochemical analyses showed a 5-fold higher photocurrent density and significantly reduced charge transfer resistance compared with pristine materials, while photoluminescence quenching confirmed efficient suppression of electron–hole recombination. Radical scavenging experiments identified superoxide radicals and holes as the dominant species, consistent with a direct Z-scheme charge transfer pathway that preserves strong redox potentials. Reusability tests over five cycles demonstrated only a minor decline in phenol degradation efficiency (from 95.2% to 88.7%), and post-reaction XRD confirmed structural stability. These results highlight the MoS_2/CdS heterostructure as a robust, high-performance photocatalyst for treating complex industrial wastewater and provide insights into rationally designing advanced Z-scheme systems for environmental remediation.

(Received September 7, 2025; Accepted December 23, 2025)

Keywords: Photocatalysis; Heterojunction design; Visible-light activation; Charge Separation; Wastewater remediation

1. Introduction

The global expansion of oil and gas exploration has led to the generation of vast quantities of produced water, which constitutes the largest waste stream by volume in the industry [1]. This wastewater is a complex and environmentally hazardous mixture, containing high concentrations of total dissolved solids, dispersed hydrocarbons, heavy metals, radionuclides, and a variety of organic compounds [2]. Furthermore, it is often laden with chemical additives used during the extraction process, including corrosion inhibitors, biocides, and surfactants, which are particularly recalcitrant and toxic to aquatic life [3]. The uncontrolled discharge of produced water can lead to severe contamination of surface and groundwater resources, disrupting ecosystems and posing

* Corresponding author: baitangtu1416@163.com
https://doi.org/10.15251/JOR.2025.216.875

significant risks to environmental sustainability. As production wells age, the water-to-oil ratio, or "water cut," invariably increases, amplifying the volume of wastewater that requires management and disposal. Conventional treatment methods, such as gravity separation, coagulation, and flotation, are effective at removing dispersed oil and suspended solids but are largely inadequate for eliminating dissolved organic contaminants and surfactants and often generate large volumes of toxic sludge.

Advanced Oxidation Processes (AOPs) have emerged as a powerful class of technologies capable of mineralizing a wide range of persistent organic pollutants into benign end-products like carbon dioxide and water [4]. Among these, heterogeneous photocatalysis is regarded as a particularly promising "green" technology due to its potential to operate under ambient temperature and pressure, utilize abundant solar energy, and avoid secondary pollutants; nevertheless, large-scale industrial application remains limited because of persistent scale-up and performance barriers [5]. Two fundamental materials limitations are widely recognized: first, benchmark photocatalysts such as TiO_2 possess a wide band gap, restricting activity to the UV portion of sunlight (≈5% of the solar spectrum) [6]; second, rapid electron–hole recombination—often on ultrafast (ps–ns) timescales—severely suppresses quantum efficiency [7].

To overcome these challenges, significant research efforts have been directed toward developing photocatalysts that can efficiently harness visible light (a major fraction of the solar spectrum). Narrow-bandgap semiconductors are prime candidates. CdS is an excellent visible-light absorber [8], while molybdenum disulfide (MoS_2), a two-dimensional transition-metal dichalcogenide, exhibits a layer-dependent band gap and presents a high density of catalytically active edge sites [9,10]. However, pristine CdS suffers from severe photocorrosion, where photogenerated holes oxidize S^{2-} to S^0 (and can lead to Cd^{2+} release), compromising stability [11]; both pristine CdS and MoS_2 also experience fast charge recombination, limiting activity [10]. Forming heterostructures is a proven strategy to mitigate these issues: coupling MoS_2 with n-type CdS can create an interfacial built-in electric field that promotes spatial charge separation and suppresses recombination, thereby enhancing photocatalytic efficiency [12].

While a conventional Type-II heterojunction can effectively separate electrons and holes, it often does so at the expense of their redox potential, as the charge carriers migrate to the lower-energy band edges of the composite system. A more advanced charge transfer pathway, the direct Z-scheme, offers a superior solution by mimicking the process of natural photosynthesis. This process preserves the highly energetic electrons in the more negative CB and the strongly oxidizing holes in the more positive VB, thus maximizing the overall redox power of the photocatalyst for degrading highly stable pollutants. This paper reports the successful synthesis of a novel MoS_2/CdS Z-scheme heterostructure. Its photocatalytic performance was tested for the mineralizing phenol and sodium dodecyl sulfate (SDS), selected as model organic and surfactant pollutants commonly found in produced water. Furthermore, the underlying Z-scheme charge transfer mechanism was elucidated through photoelectrochemical measurements and reactive oxygen species trapping experiments.

2. Materials and Methods

Pristine CdS nanorods were synthesized via a hydrothermal method adapted from a previous report [13]. Pure MoS_2 nanosheets were prepared using a hydrothermal method [14]. The MoS_2/CdS heterostructures were synthesized via a hydrothermal method to ensure intimate interfacial contact. First, 500 mg CdS nanorods were dispersed in DI water. Subsequently, calculated amounts of $(NH_4)_6\ Mo_7O_{24}{\cdot}4H_2O$ and L-cysteine were added to the suspension to achieve theoretical weight percentages of MoS_2 of 2%, 5%, and 8%. L-cysteine served as the sulfur source for the in-situ growth of MoS_2 on the CdS surface. The mixture was stirred for 60 minutes to ensure

complete dissolution and adsorption of the precursors onto the CdS nanorods. After the reaction, the product was separated. The final composite samples were denoted as 2%-MC, 5%-MC, and 8%-MC, corresponding to the theoretical weight percentage of MoS_2.

The photocatalytic ability of products was tested by the mineralizing phenol and SDS in a simulated produced water matrix. In a typical experiment, 50 mg of the photocatalyst was dispersed into an aqueous solution containing 20 mg/L of phenol and 10 mg/L of SDS. At specific time intervals during irradiation, 3 mL aliquots were withdrawn and the absorbance peak at 270 nm. The mineralization of SDS was quantified by measuring the TOC.

To identify the primary reactive species, scavenger experiments were performed with the optimal 5%-MC catalyst. 1 mM of isopropanol (IPA), p-benzoquinone (BQ), or AO was added to the reaction solution to quench $^{\bullet}OH$, $^{\bullet}O_2^-$, and h^+, respectively [15]. The stability and reusability of the 5%-MC photocatalyst were evaluated by conducting five consecutive cycles of phenol degradation.

3. Results and discussion

The diffraction pattern (Fig. 1) of pure CdS exhibits well-defined peaks at 2θ values of 24.7°, 26.3°, 28.4°, 43.6°, 47.7°, and 51.9°, which can be indexed to the hexagonal wurtzite phase of CdS (JCPDS No. 41-1049). The sharpness of the peaks indicates good crystallinity. The XRD pattern for pure MoS_2 displays characteristic peaks at 14.4°, 32.7°, and 58.4°, corresponding to the hexagonal 2H-MoS_2 phase (JCPDS No. 87-2416) [16]. For the 2%-MC, 5%-MC, and 8%-MC composites, all the major peaks can be readily assigned to the hexagonal CdS phase. Notably, no distinct diffraction peaks corresponding to MoS_2 are observed, particularly in the low-loading samples (2%-MC and 5%-MC). This phenomenon does not suggest an unsuccessful synthesis but rather indicates that the MoS_2 component is present in a very low quantity, is highly dispersed on the surface of the CdS nanorods, or possesses a low degree of crystallinity, preventing the formation of detectable diffraction peaks [13]. This observation is a positive indicator of the formation of a highly integrated heterostructure rather than a simple physical mixture of two crystalline phases.

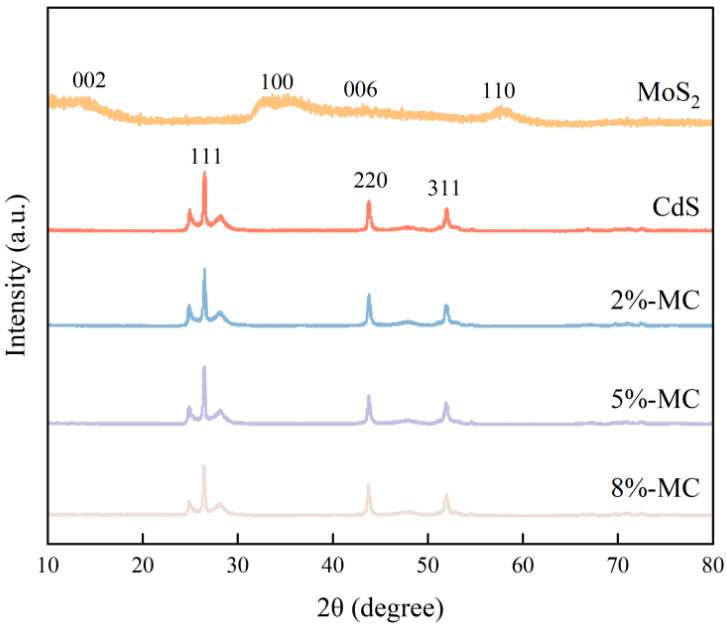

Fig. 1. XRD patterns of pure CdS, pure MoS_2, 2%-MC, 5%-MC, and 8%-MC photocatalysts.

The SEM image of pure CdS (Fig. 2a) reveals a uniform morphology consisting of aggregated nanorods with diameters ranging from 10 to 50 nm. Pure MoS_2 (Fig. 2b) exhibits a flower-like structure composed of interconnected, ultrathin nanosheets. For the 5%-MC composite (Fig. 2c, d), the overall nanorod morphology of CdS is well-preserved, but the surface appears significantly rougher due to the decoration with MoS_2 nanosheets.

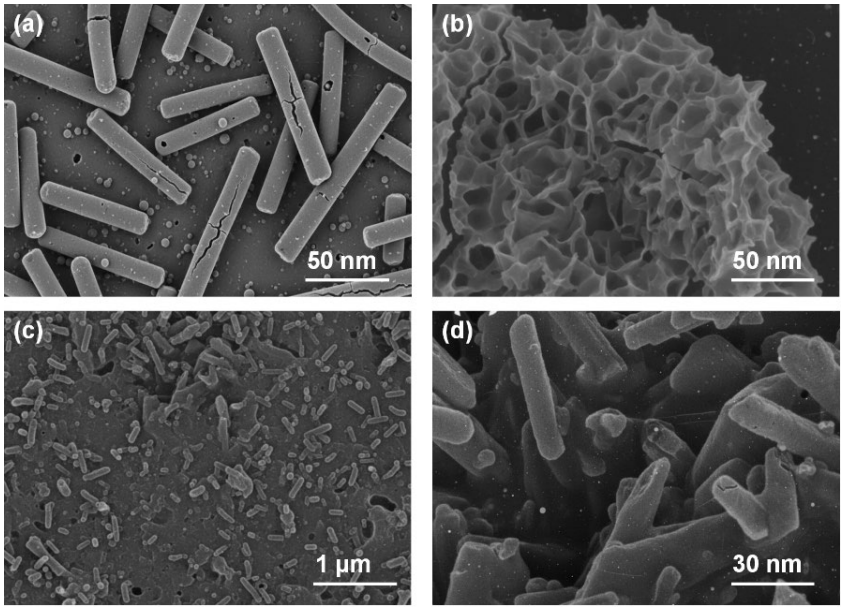

Fig. 2. SEM images of (a) pure CdS, (b) pure MoS_2, (c) 5%-MC composite at low magnification, and (d) 5%-MC composite at high magnification.

Further microstructural details were obtained from TEM analysis. Fig. 3a shows a TEM image of an individual CdS nanorod, confirming its solid, rod-like structure. Fig. 3b displays an ultrathin, sheet-like morphology for the synthesized MoS_2. The TEM image of the 5%-MC composite (Fig. 4a) provides direct evidence of the heterostructure formation, where few-layered MoS_2 nanosheets are intimately anchored onto the surface of a CdS nanorod. HRTEM image in Fig. 4b clearly visualizes the interfacial region between the two components [16]. The seamless contact between these two distinct crystalline domains confirms the formation of an intimate heterojunction at the atomic level, which is crucial for efficient charge transfer.

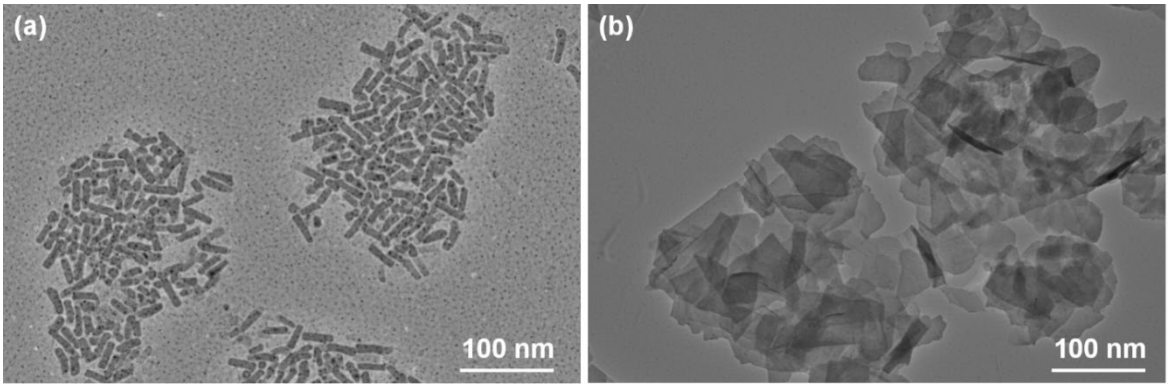

Fig. 3. TEM images of (a) a single pure CdS nanorod and (b) pure MoS2 nanosheets.

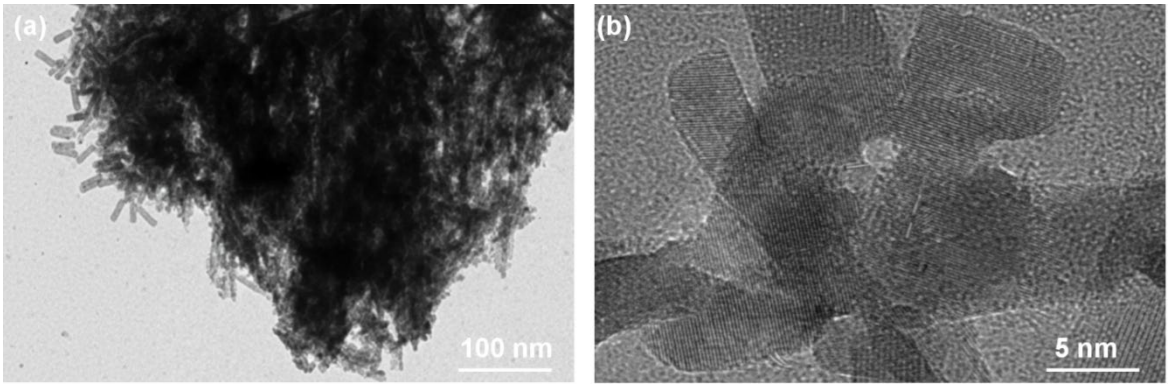

Fig. 4. (a) TEM image of the 5%-MC heterostructure, (b) HRTEM image showing the interface between CdS and MoS_2.

The isotherms for pure CdS, pure MoS_2, and the 5%-MC composite are displayed in Fig. 5a. All samples exhibit a Type IV isotherm with a distinct H3 hysteresis loop with slit-like pores formed by the aggregation of plate-like particles [17]. The corresponding physicochemical properties are summarized in Table 1. The specific surface area (SSA) of the 5%-MC composite was calculated to be 68.5 m^2/g, which is significantly larger than that of pure CdS (42.1 m^2/g) and pure MoS_2 (27.8 m^2/g). This substantial increase in SSA is attributed to the hierarchical nanostructure formed by the ultrathin MoS_2 nanosheets grown on the CdS nanorods. The higher SSA can provide more active sites for the adsorption of pollutant molecules and the subsequent photocatalytic reactions, which is expected to contribute to its enhanced performance.

Fig. 5b shows the DRS spectra. The pure CdS exhibits a steep absorption edge at approximately 520 nm. Pure MoS_2 shows broad absorption across the entire visible and near-infrared regions, which is characteristic of its narrow band gap. For the MC composites, the introduction of MoS_2 leads to a significant enhancement in light absorption intensity across the visible spectrum compared to pure CdS. The absorption intensity systematically increases, indicating that the heterostructure possesses superior light-harvesting capability. The Eg of the pristine semiconductors were estimated from Tauc plots derived from the DRS data. The band gaps of CdS and MoS_2 were determined to be approximately 2.38 eV and 1.75 eV, respectively [15]. The enhanced visible light absorption of the MC composites is beneficial for generating a larger number of electron-hole pairs, which is a prerequisite for high photocatalytic efficiency.

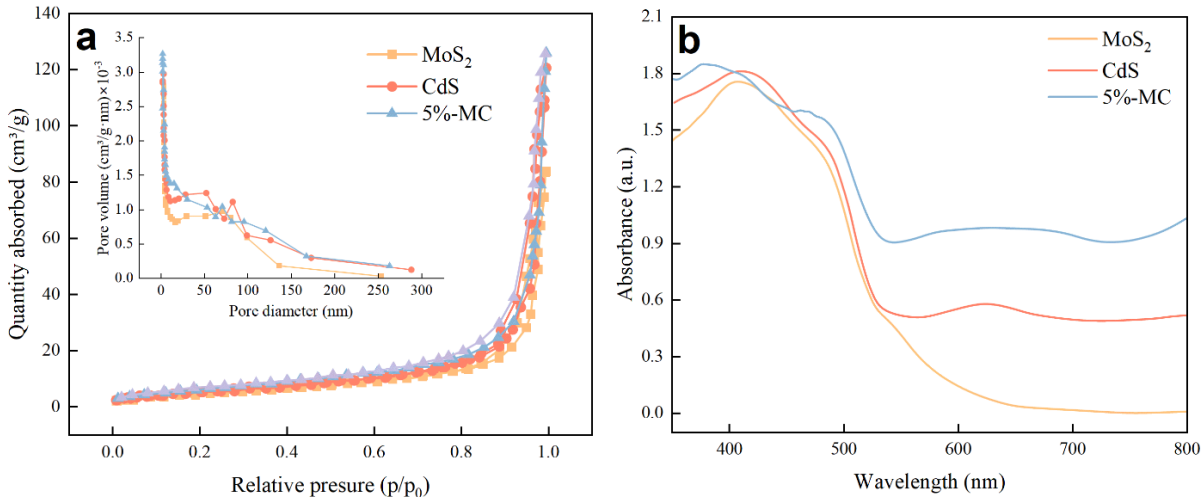

Fig. 5. (a) Nitrogen adsorption-desorption isotherms and (inset) BJH pore size distribution plots for CdS, MoS_2, and the 5%-MC composite. (b) UV-vis diffuse reflectance spectra of CdS, MoS_2, and the MC composites.

Table 1. Physicochemical properties of the synthesized photocatalysts.

Sample	BET Surface Area (m^2/g)	Average Pore Size (nm)	Band Gap (Eg, eV)
Pure CdS	42.1	12.4	2.38
Pure MoS_2	27.8	8.9	1.75
2%-MC	55.3	11.8	-
5%-MC	68.5	11.2	-
8%-MC	61.7	10.9	-

The XPS survey spectrum (Fig. 6a) confirms the presence of Cd, Mo, S, and C elements. No additional impurities were identified. In the Cd 3d spectrum (Fig. 6b), two well-defined peaks appear at binding energies of 405.1 eV and 411.8 eV. These peaks are attributed to the Cd $3d_{5/2}$ and Cd $3d_{3/2}$ spin–orbit components, respectively, verifying that cadmium exists in the +2 oxidation state within CdS [18]. The S 2p spectrum (Fig. 6c) is fitted with two main doublets. The peaks at 161.6 eV and 162.8 eV are attributed to S $2p_{3/2}$ and S $2p_{1/2}$ of S^{2-} ions in the metal-sulfur bonds of both CdS and MoS_2. The Mo 3d spectrum (Fig. 6d) can be deconvoluted into two peaks at 229.2 eV and 232.3 eV, which are assigned to Mo $3d_{5/2}$ and Mo $3d_{3/2}$, respectively. These binding energies are characteristic of the Mo^{4+} state in MoS_2 [19]. This shift in binding energies is direct evidence of a strong electronic interaction and charge redistribution at the heterojunction interface. This confirms that electrons are transferred from CdS to MoS_2 upon the formation of the heterojunction, which is a key feature supporting the proposed charge transfer mechanism.

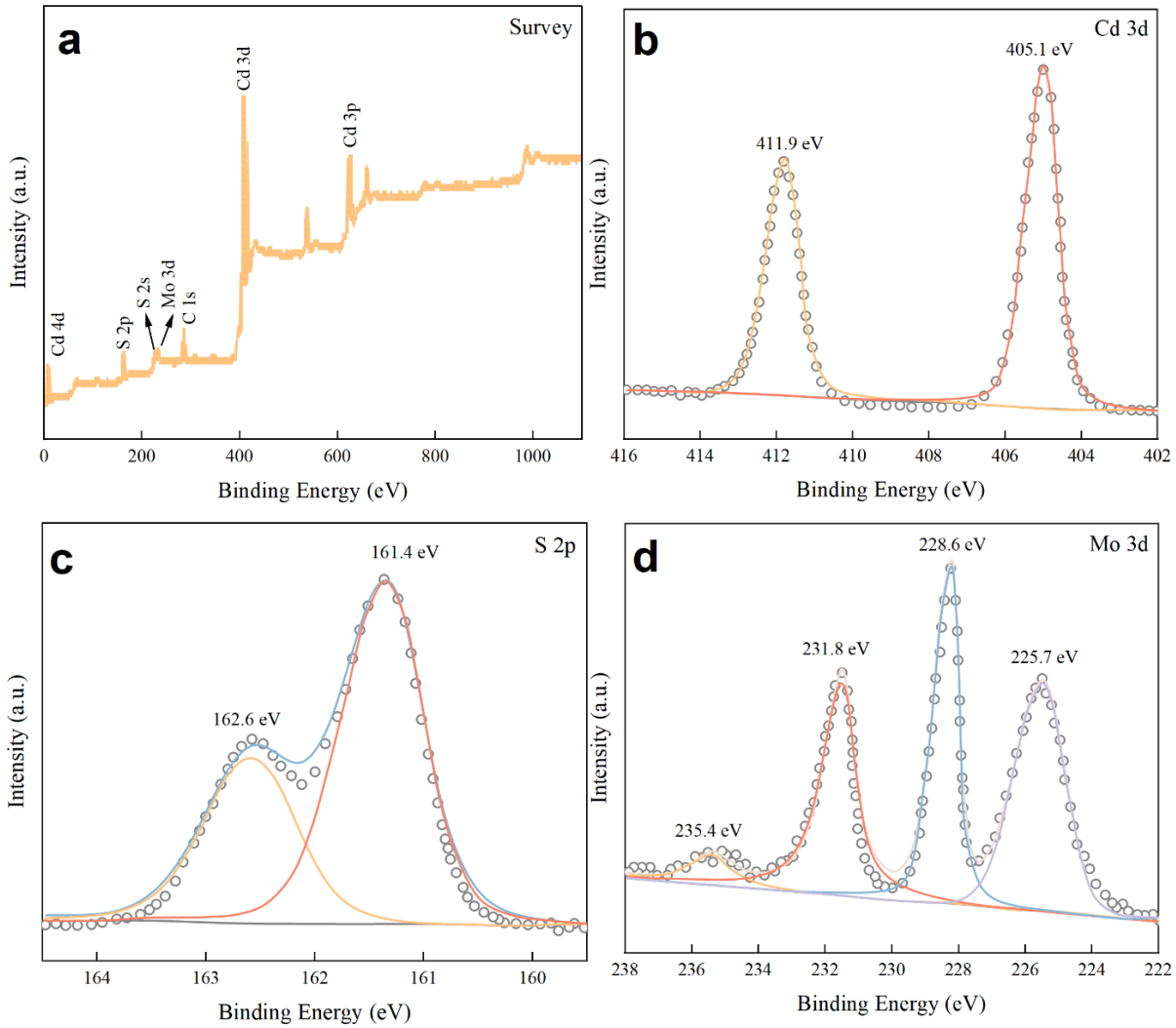

Fig. 6. (a) XPS survey spectrum of the 5%-MC composite. (b) Cd 3d, (c) S 2p, and (d) Mo 3d for the 5%-MC composite.

As shown in Fig. 7, the 5%-MC composite exhibited the highest adsorption capacity for both phenol (~15%) and SDS (~12%), which is consistent with its larger SSA. The photocatalytic degradation profiles are presented in Fig. 8. Control experiments confirmed that negligible degradation occurred in the absence of a catalyst (photolysis) or in the absence of light (adsorption in the dark). Both pure CdS and pure MoS_2 showed modest photocatalytic activity, achieving around 45% and 30% degradation of phenol in 120 minutes, respectively. In contrast, all MC composites demonstrated significantly enhanced performance. The photocatalytic activity followed the order: 5%-MC > 8%-MC > 2%-MC > Pure CdS > Pure MoS_2. The optimal 5%-MC composite achieved a remarkable degradation efficiency of 95.2% for phenol and 81.5% TOC removal for SDS within 120 minutes.

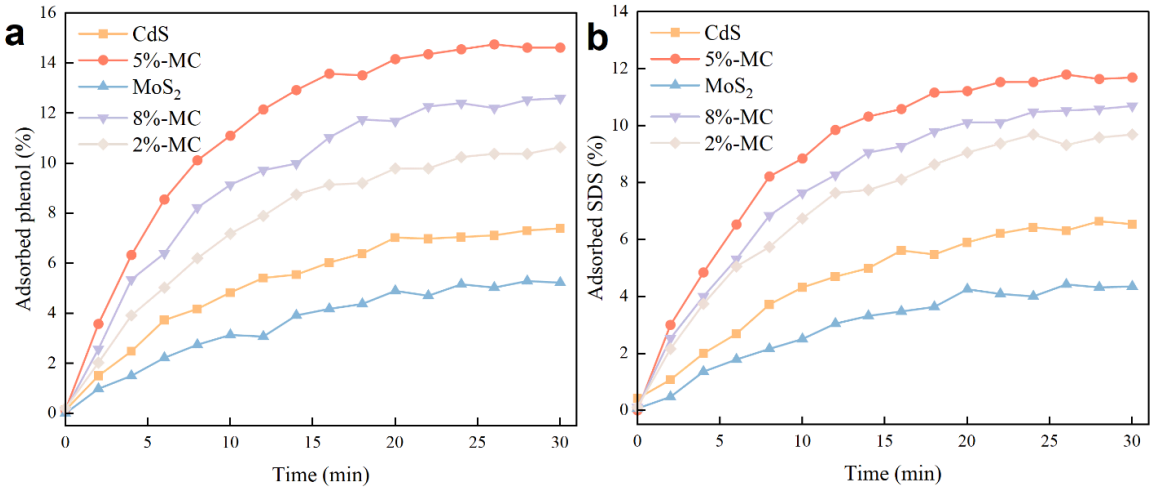

Fig. 7. Adsorption of (a) phenol and (b) SDS by the different photocatalysts in the dark.

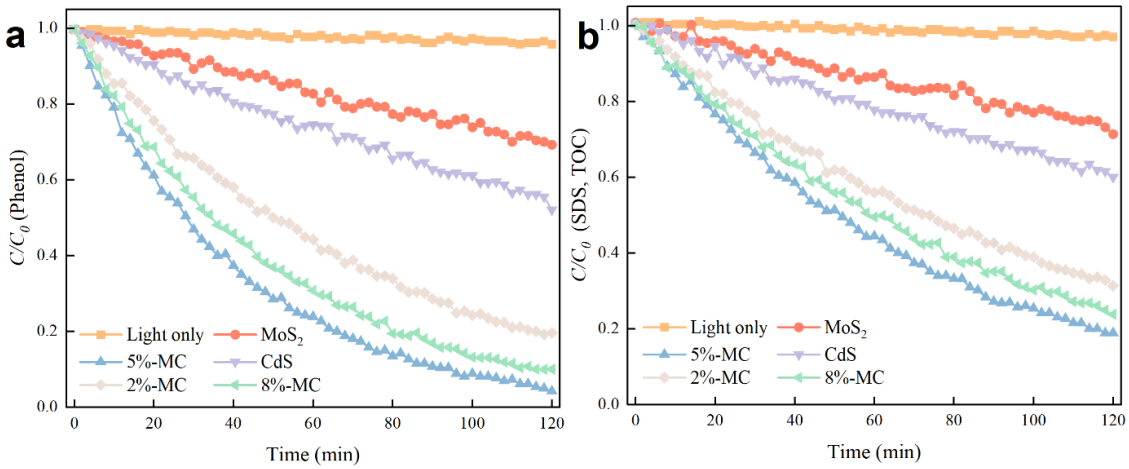

Fig. 8. Photocatalytic degradation curves (C/C0 vs. time) for (a) phenol and (b) SDS under visible light irradiation.

The degradation kinetics of both pollutants were found to fit well with the pseudo-first-order kinetic model. This superior performance of 5%-MC highlights the synergistic effect of forming the MoS_2/CdS heterostructure. The existence of an optimal MoS2 loading at 5 wt% is evident. While increasing the MoS_2 content from 2% to 5% enhances the formation of efficient heterojunctions and active sites, a further increase to 8% leads to a slight decrease in activity. This can be attributed to two factors: excessive MoS_2 can block the absorption of light by the underlying CdS, and aggregation of MoS_2 nanosheets at higher concentrations may create charge recombination centers, thereby reducing the overall quantum efficiency.

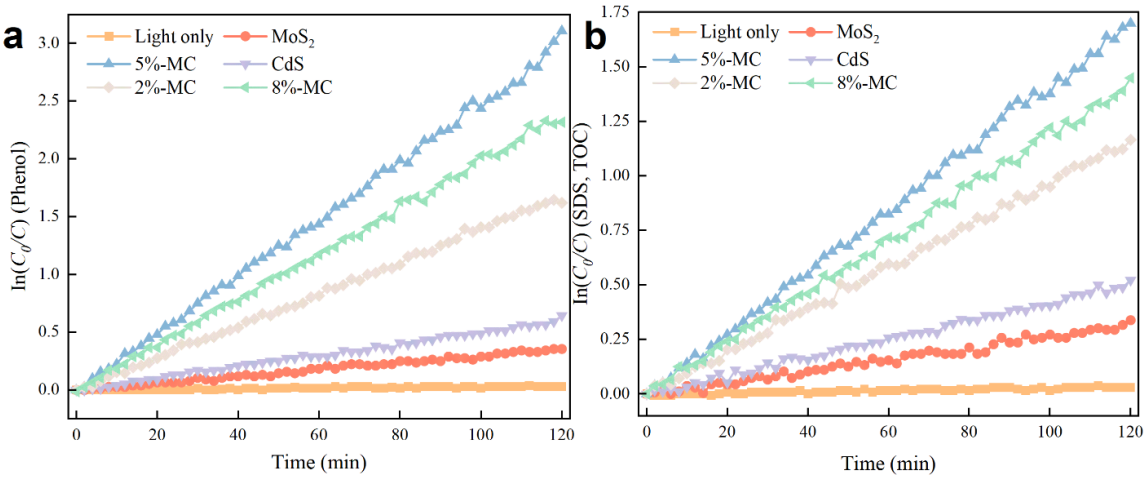

Fig. 9. Pseudo-first-order kinetic plots for the degradation of (a) phenol and (b) SDS.

Table 2. Kinetic parameters for the degradation of phenol and SDS.

Catalyst	Pollutant	Rate Constant, k (min−1)	Correlation Coefficient (R^2)
Pure CdS	Phenol	0.0050	0.991
Pure MoS_2	Phenol	0.0030	0.985
2%-MC	Phenol	0.0138	0.994
5%-MC	Phenol	0.0245	0.998
8%-MC	Phenol	0.0196	0.996
5%-MC	SDS (TOC)	0.0140	0.992

The charge carrier separation and transfer dynamics were investigated. Fig. 10a shows the photoluminescence (PL) spectra of CdS and the 5%-MC composite. CdS exhibits a strong emission peak centered at around 540 nm. In stark contrast, the PL intensity of the 5%-MC composite is significantly quenched. Since PL emission is a direct result of charge recombination, this pronounced quenching provides strong evidence that the formation of the MoS_2/CdS heterojunction effectively suppresses electron-hole recombination, leading to a higher availability of charge carriers for photocatalytic reactions [20].

The efficiency of charge separation and transport was further evaluated by photoelectrochemical measurements. The photocurrent responses of CdS, MoS_2, and 5%-MC electrodes were recorded under several on-off cycles (Fig. 10b). The 5%-MC electrode generated a photocurrent density that was remarkably higher (approximately 5-fold) and more stable than that of either pure CdS or pure MoS_2. This indicates that the heterostructure facilitates more efficient separation of photogenerated charges and promotes their transfer to the electrode surface [16].

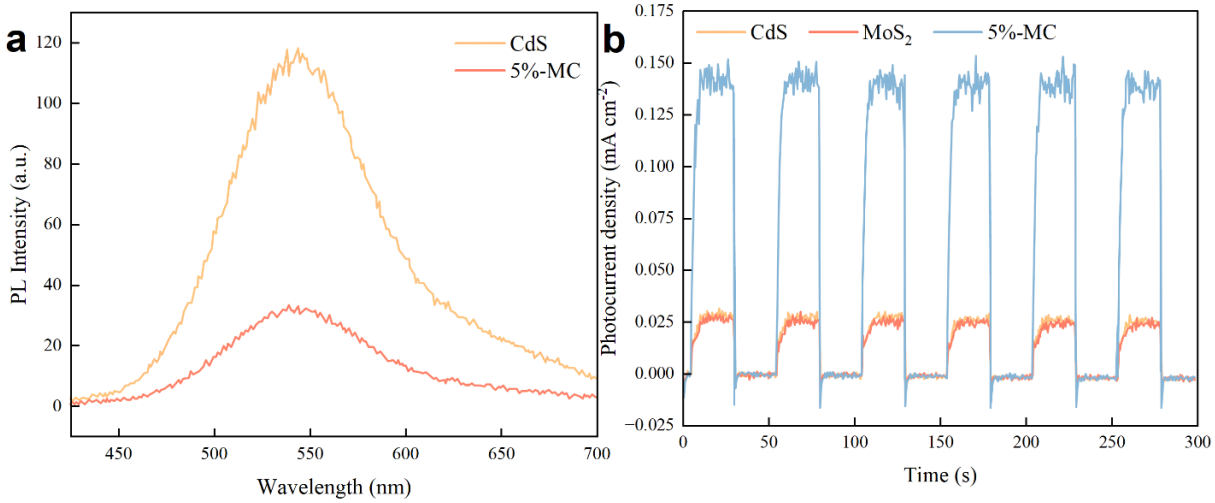

Fig. 10. (a) PL spectra of CdS and the 5%-MC composite. (b) Photocurrent response curves of CdS, MoS_2, and 5%-MC electrodes under chopped visible light irradiation.

Based on the characterization results and band theory, a direct Z-scheme charge transfer mechanism is proposed as illustrated in Fig. 11. The CB and VB edge potentials of CdS and MoS_2 were calculated [21]. The calculated potentials vs. NHE are: ECB = –0.51 eV and EVB = +1.87 eV for CdS, and ECB = +0.20 eV and EVB = +1.95 eV for MoS_2. Under visible light irradiation, both CdS and MoS_2 are excited, generating electron-hole pairs. Due to the intimate contact and the established internal electric field, the photogenerated electrons in the CB of MoS_2 (+0.20 eV) migrate and recombine with the holes. This recombination pathway effectively removes the less useful charge carriers. The preserved electrons in the CdS CB are sufficiently energetic to reduce adsorbed oxygen to form superoxide radicals, as the redox potential of $O_2/^{\bullet}O_2^-$ is –0.33 eV vs. NHE. Simultaneously, the holes accumulated in the MoS_2 VB possess a very high oxidation potential, enabling them to directly oxidize the adsorbed organic pollutants or react with water to a lesser extent.

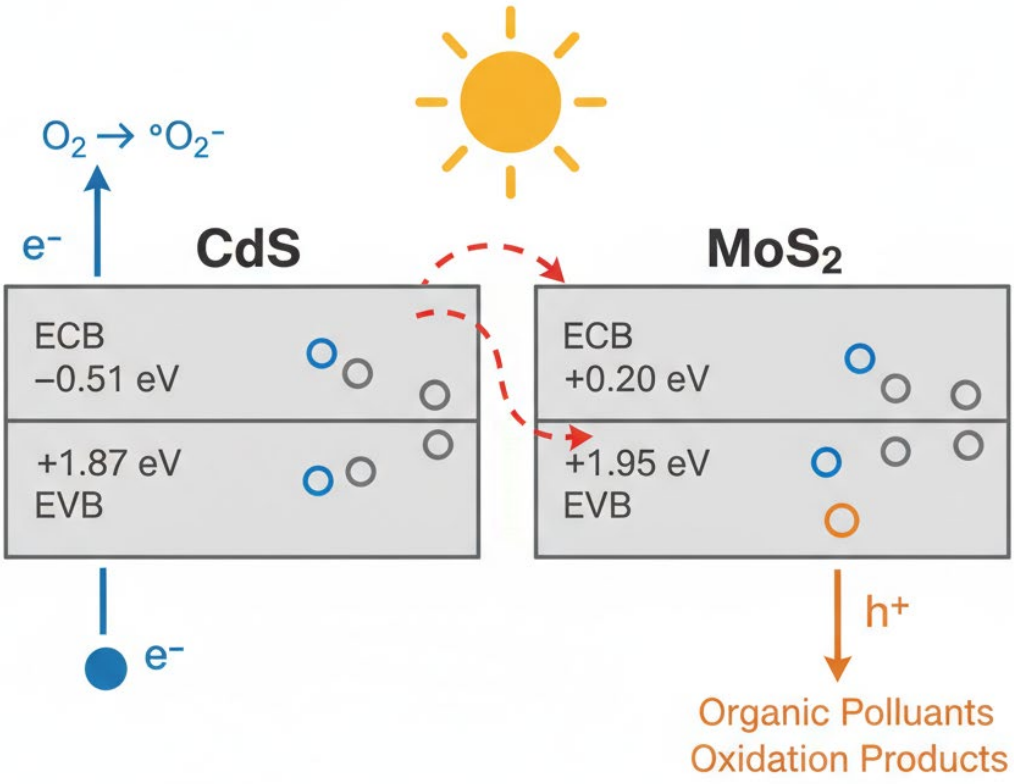

Fig. 11. Schematic illustration of the direct Z-scheme charge transfer mechanism in the MoS_2/CdS heterostructure.

The stability of the optimal 5%-MC composite was evaluated by performing five consecutive cycles of phenol degradation under the same conditions. As shown in Fig. 12, the catalyst maintained high activity throughout the cycling test. The degradation efficiency decreased only slightly, from 95.2% in the first cycle to 88.7% in the fifth cycle. This minor loss in activity could be due to the inevitable mass loss of the catalyst during the recovery process between cycles. To further confirm its structural stability, the XRD pattern of the 5%-MC catalyst was measured after the fifth cycle. The pattern shows no discernible changes, indicating that the crystalline structure of the composite remained intact and that no significant photocorrosion or phase transformation occurred during the photocatalytic process.

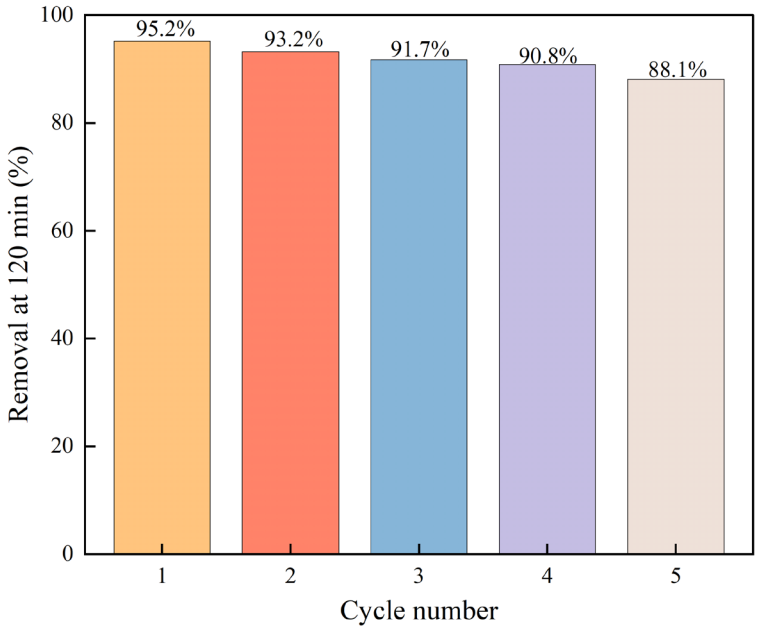

Fig. 12. Reusability test of the 5%-MC photocatalyst for the degradation of phenol over five consecutive cycles.

4. Conclusions

In summary, a series of novel MoS_2/CdS heterostructures was successfully synthesized. Comprehensive characterization confirmed the formation of an intimate heterojunction where ultrathin MoS_2 nanosheets were uniformly decorated on the surface of CdS nanorods. Among the prepared composites, the sample with an optimal loading of 5 wt% MoS_2 (5%-MC) exhibited outstanding photocatalytic performance, significantly surpassing the activity of pristine CdS and MoS_2. The calculated pseudo-first-order rate constant for phenol degradation over 5%-MC was 4.9 and 8.2 times higher than that of pure CdS and MoS_2, respectively. The substantially enhanced photocatalytic activity was attributed to the synergistic effects within the heterostructure. Crucially, the formation of a direct Z-scheme heterojunction was identified as the primary mechanism for the performance enhancement. This was rigorously supported by photoluminescence, photoelectrochemical measurements, and reactive species trapping experiments, which collectively demonstrated that the Z-scheme pathway effectively promotes the separation of photogenerated charge carriers while preserving their strong intrinsic redox potentials. The dominant reactive species were identified as superoxide radicals and holes, consistent with the charge distribution predicted by the Z-scheme model. Furthermore, the 5%-MC catalyst exhibited excellent stability and reusability, maintaining high degradation efficiency over five consecutive cycles without significant structural degradation. This work not only presents a highly efficient and robust photocatalyst for the remediation of complex organic pollutants in produced water but also provides a clear design strategy for developing advanced Z-scheme heterostructures for challenging environmental applications.

Availability of Data and Materials

The data that support the findings of this study are available from the corresponding author upon reasonable request

Author Contributions

The authors confirm contribution to the paper as follows: study conception and design: Y.L., X.C.; data collection: Y.L.; analysis and interpretation of results: Z.W.; draft manuscript preparation: X.C. and Y.L. All authors reviewed the results and approved the final version of the manuscript.

Acknowledgment

Not applicable

Funding

Not applicable

Conflict of Interest

The authors declare no conflicts of interest to report regarding the present study.

References

[1] T. F. Jaramillo, K. P. Jørgensen, J. Bonde, J. H. Nielsen, S. Horch, I. Chorkendorff, Science **317**(5834), 100-102 (2007). https://doi.org/10.1126/science.1141483

[2] F. Nath, M. O. S. Chowdhury, M. M. Rhaman, Water **15**(23), 4088 (2023). https://doi.org/10.3390/w15234088

[3] E. T. Igunnu, G. Z. Chen, International Journal of Low-Carbon Technologies **9**(3), 157-177 (2014). https://doi.org/10.1093/ijlct/cts049

[4] F. Chen, Y. Wei, M. Ren, S. Sun, S. Ghosh, R. V. Kumar, ChemCatChem **16**(8), e202301492 (2024). https://doi.org/10.1002/cctc.202301492

[5] S. K. Nadikatla, V. B. Chintada, T. R. Gurugubelli, R. Koutavarapu, Molecules **28**(11), 4277 (2023). https://doi.org/10.3390/molecules28114277

[6] M. A. Lazar, S. Varghese, S. S. Nair, Catalysts **2**(4), 572-601 (2012). https://doi.org/10.3390/catal2040572

[7] K. Ozawa, M. Emori, S. Yamamoto, R. Yukawa, S. Yamamoto, R. Hobara, K. Fujikawa, H. Sakama, I. Matsuda, Journal of Physical Chemistry Letters **5**(11), 1953-1957 (2014). https://doi.org/10.1021/jz500770c

[8] J. A. Nasir, Z. ur Rehman, S. N. A. Shah, A. Khan, I. S. Butler, C. R. A. Catlow, Journal of Materials Chemistry A **8**(40), 20752-20780 (2020). https://doi.org/10.1039/D0TA06069A

[9] J. Beyer, A. Goksøyr, D. Ø. Hjermann, J. Klungsøyr, Marine Environmental Research **162**, 105155 (2020). https://doi.org/10.1016/j.marenvres.2020.105155

[10] S. A. Shah, I. Khan, A. Yuan, Molecules **27**(10), 3289 (2022). https://doi.org/10.3390/molecules27103289

[11] Y. Chen, W. Zhong, F. Chen, P. Wang, J. Fan, H. Yu, Journal of Materials Science and Technology **121**, 19 (2022). https://doi.org/10.1016/j.jmst.2021.12.051

[12] X. Zong, G. Wu, H. Yan, G. Ma, J. Shi, F. Wen, L. Wang, C. Li, Journal of Physical Chemistry C **114**(4), 1963-1968 (2010). https://doi.org/10.1021/jp904350e

[13] X. Liu, J. Li, W. Yao, ACS Omega **5**(42), 27463-27469 (2020). https://doi.org/10.1021/acsomega.0c03968

[14] D. Dong, W. Yan, Y. Tao, Y. Liu, Y. Lu, Z. Pan, Materials **16**(11), 4030 (2023). https://doi.org/10.3390/ma16114030

[15] A. Rahman, F. Khan, J. R. Jennings, A. L. Tan, Y.-M. Kim, M. M. Khan, BMC Chemistry **18**(1), 135 (2024).

https://doi.org/10.1186/s13065-024-01250-y

[16] G. He, Y. Zhang, Q. He, Catalysts **9**(4), 379 (2019).https://doi.org/10.3390/catal9040379

[17] K. Shi, E. E. Santiso, K. E. Gubbins, in Porous Materials: Theory and Its Application for Environmental Remediation (Eds: J. C. Moreno-Piraján, L. Giraldo-Gutierrez, F. Gómez-Granados), Springer International Publishing, Cham, 315-340 (2021). https://doi.org/10.1007/978-3-030-65991-2_12

[18] S. Li, W. Huang, P. Yang, Z. Li, B. Xia, M. Li, C. Xue, D. Liu, Science of the Total Environment **754**, 141925 (2021). https://doi.org/10.1016/j.scitotenv.2020.141925

[19] J. Liu, Y. Yang, J. Bai, H. Wen, F. Chen, B. Wang, Analytical Chemistry **90**(5), 3621-3627 (2018). https://doi.org/10.1021/acs.analchem.8b00239

[20] K. Hamid, M. Z. B. Mukhlish, M. T. Uddin, RSC Advances **14**(54), 38908-38923 (2024). https://doi.org/10.1039/D4RA07156J

[21] A. İ. Vaizoğullar, Journal of Inorganic and Organometallic Polymers and Materials **30**(10), 4129-4141 (2020). https://doi.org/10.1007/s10904-020-01563-0